VINAG: A HIGHLY INTEGRATED SYSTEM FOR AUTONOMOUS ON-BOARD ABSOLUTE AND RELATIVE SPACECRAFT NAVIGATION

Vincenzo Capuano [(1)], Giovanni Cuciniello [(2)], Vincenzo Pesce [(3)], Roberto Opromolla[(4)], Salvatore Sarno[(4)], Michelle Lavagna [(3)], Michele Grassi[(4)], Federico Corraro [(2)], Giuseppe Capuano [(1)], Paolo Tabacco[(5)], Francesco Meta[(5)], Maria Libera Battagliere [(6)], Alberto Tuozzi[(6)]

[(1)] Techno System Dev. S.r.l., Via Provinciale Pianura 2, San Martino Zona Industriale, 80078 Pozzuoli Italy, vcapuano@tsd-space.it, gcapuano@tsd-space.it

[(2)]Centro italiano ricerche aerospaziali (CIRA s.c.p.a.), Via Maiorise 1, 81043 Capua CE, Italy, g.cuciniello@cira.it, f.corraro@cira.it

[(3)]Politecnico di Milano, Aerospace Science and Technology Department, via La Masa, 34, 20156 Milano, Italy, vincenzo.pesce@polimi.it, michelle.lavagna@polimi.it

[(4)]University of Naples "Federico II", Dept. of Industrial Engineering, P.le Tecchio 80, 80125, Napoli, Italy, roberto.opromolla@unina.it, salvatore.sarno@unicampania.it, michele.grassi@unina.it

[(5)]Space Technology S.r.l., Via dell'Orsa Maggiore, 21, 00144 Roma, Italy, tabacco@spacetechnology.it, meta@ spacetechnology.it

[(6)]Agenzia Spaziale Italiana (ASI), Via del Politecnico snc, 00133 Roma, Italy, maria.battagliere@asi.it

1. ABSTRACT

VINAG (VISION/INS integrated Navigation Assisted by GNSS) is a highly integrated system, specifically designed for autonomous on-board navigation in a wide class of space missions, which include, along the operational lifetime, proximity among heterogeneous space segments. The system VINAG is under development by a team of Italian companies and universities, co-financed by the Italian Space Agency. In particular, thanks to a high level of integration of its subsystems, VINAG, is a low mass, low volume and low power device, suitable for small and very small satellites. The complete system integrates a Cameras Subsystem (a monocular camera and a Star sensor), an Inertial Measurement Unit (IMU) and a GNSS (Global Navigation Satellite System) receiver, in order to provide both 1) absolute orbit and attitude determination and 2) relative position and attitude determination with respect to an orbiting non-cooperative object. In this paper, we present the whole system VINAG, focusing first on its functional architecture, second on the adopted navigation and data fusion algorithms and third briefly on its hardware (HW) design. The camera system and the GNSS receiver developed for VINAG, respectively by TSD Space and by Space Technology are also described in short. In addition, preliminary simulations that assess the potential performance of VINAG, in LEO (Low Earth Orbit) and GEO (Geostationary Orbit) are described.

2. INTRODUCTION

Navigation is an essential process in all satellite missions, often having a strong impact on their success. Over the last decades, several technologies have been adopted for spacecraft navigation. It is intuitive that a combination of these that sums their advantages and compensate their limitations, can provide the best achievable performance to the resultant integrated system. In space applications that require considerable autonomy, precision, robustness, adaptability to several scenarios, as

missions of On-Orbit Servicing (OOS), debris removal, or in general in missions where a swarm or formation of spacecraft is involved, the integration of more metrology systems (integrated navigation) can certainly be more effective than using a single technology individually. In addition, it is also intuitive that "integration" means mass and volume saving, as well as energy saving. If the individual subsystems are already designed and conceived to be integrated in one bigger system, it is possible to avoid non-efficient replication of hardware (HW) components and basic functionalities, as computing, power supply, data interface, etc., with a consequent reduction of the total mass, volume and power consumption.

VINAG (VISION/INS integrated Navigation Assisted by GNSS) is a highly integrated system, specifically designed for autonomous on-board navigation in a wide class of space missions, which include, along the operational lifetime, proximity among heterogeneous space segments. The complete system integrates a Cameras Subsystem (a monocular camera and a Star sensor), an Inertial Measurement Unit (IMU) and a GNSS (Global Navigation Satellite System) receiver, in order to provide both 1) absolute orbit and attitude determination and 2) relative position and attitude determination with respect to an orbiting non-cooperative object. With a modular architecture, VINAG can be used in different configurations. The VINAG HW is composed by the VINAG Central Unit (VCU), the VINAG Cameras System and the Inertial Navigation System (INS) Module (which contains the IMU). The Cameras System includes the CMOS monocular camera and the Star sensor, while the central unit of VINAG includes the VISNAV (VISion-based NAVigation) & Data Fusion Module (VDFM), the VISNAV HW acceleration module, the GNSS Receiver Module and the Power Conditioning & Distribution Module (PCDM).

Among the state-of-the-art integrated systems for spacecraft navigation, so far adopted in current missions or at least proposed in the literature, we can mainly find either systems for absolute navigation, based on the GNSS/INS integration with different level of tightness (loose, tight, ultra-tight, deep) or systems for relative navigation based on the integration of optical sensors. This is also confirmed by the "European Space Agency (ESA) technical dossier of AOCS sensors and actuators" [1], where mentioned examples of the state of the art GNSS/INS based integrated systems are the European Launcher Localization Kit (EL2K), the HiNAV tightly-coupled breadboard [2], the Autonomous Localization and Telemetry Sub System (ALTS S/S) [3] and the GPS/INS integrated system SIGI [4] of Honeywell. In addition, it is important also to mention that, although originally designed for earth users and currently also adopted in LEO, recent studies have demonstrated that nowadays GNSS can be used to navigate also in higher earth orbits, as MEO, GEO, HEO and beyond up to the Moon altitude [5], [6], [7]. A GPS Space Service Volume has been indeed already defined [8]. Instead, most of the optical navigation systems that have been developed or proposed, are typically not that versatile, but suitable only for a single application (e.g NAVCAM on Rosetta), since they have been one-off custom designed for a specific task and mission. A few multipurpose and versatile optical systems can be mentioned, as the generic multi-mission vision-based navigation (VisNav) chain architecture [9], the system VIBANASS (VIsion-BAsed NAvigation Sensor System) [11] and the vision-based navigation systems of Ball Aerospace for the Orion program.
To our knowledge, combining GNSS, INS and Vision in the same unit, to provide both absolute and relative orbit and attitude determination appears to be a novel solution, aligned with the current trend (according to [1]) towards multi-purpose navigation systems, robust, versatile, and adaptable to different space scenarios with different navigation requirements.

The rest of the paper is organized as follows. Section 3 illustrates the high level functional architecture of VINAG. Section 4 details the algorithms implemented both for absolute navigation and for relative navigation. In Section 5 a summary of the hardware design is also provided. While Section 6 describes

preliminary simulations of the navigation performance of VINAG as well as the adopted parametric models and assumptions. Finally in Section 7 the conclusions are drawn.

3. HIGH LEVEL ARCHITECTURE

The high level functional architecture of VINAG is illustrated in Figure 1. By means of a nonlinear Kalman filter, for absolute orbit determination, GNSS observations are fused with inertial measurements and with a model of the absolute dynamics; inertial angular measurements are also combined with Star sensor-based attitude estimates for absolute attitude determination. While, in relative navigation, images of a target orbiting object are collected by a monocular CMOS camera to provide vision-based pose (position and attitude) estimates, then filtered with a model of their relative dynamics.

The proposed architecture also requires further inputs related to the target geometry and to the configuration of the navigation algorithms (e.g. selection between absolute or relative navigation modes). Moreover, the internal functional status of the navigation system is also outputted (sensor diagnostics, validity, estimated accuracies, etc.).

A more detailed discussion on the algorithms structure is reported in the following sections.

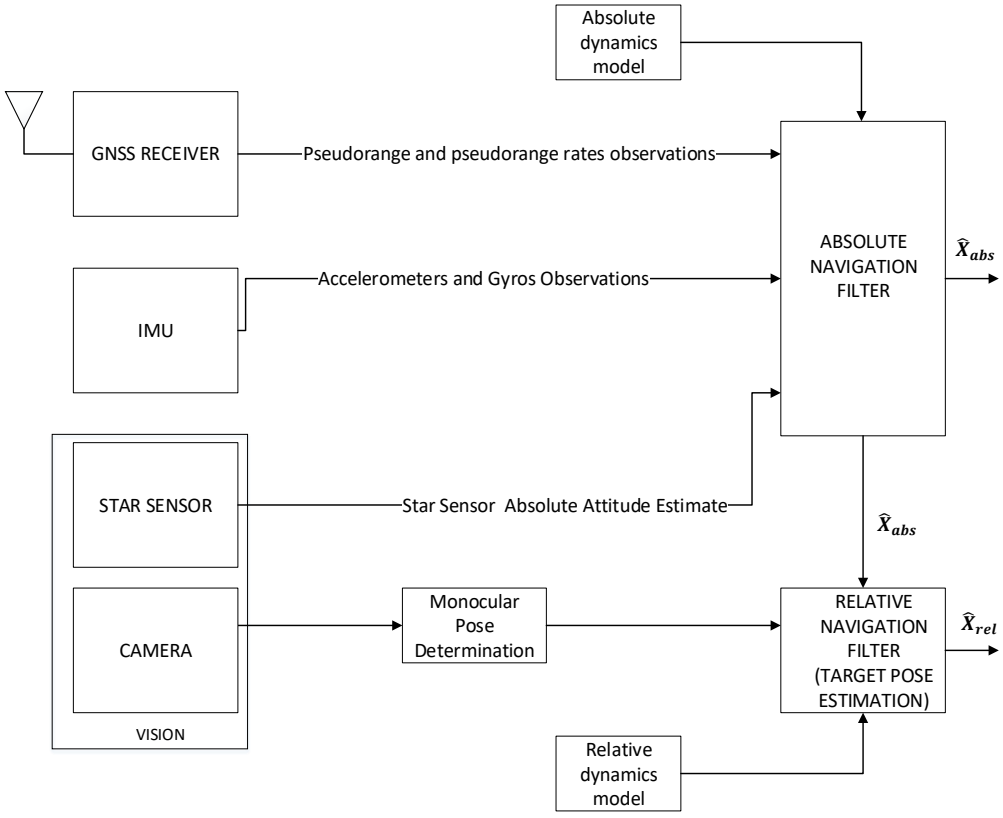

Figure 1. High level functional architecture.

4. NAVIGATION AND DATA FUSION IMPLEMENTATION

In this section, the algorithms implemented for both absolute and relative navigation are described in detail.

3.1 Absolute Navigation

The integration of GNSS, IMU and Star sensor observations enables orbit and attitude determination. The following sections describe in detail the implementation of a GNSS/INS/Star sensor – based orbital filter.

GNSS/INS/Star sensor-based orbital filter

The Absolute Navigation algorithm is the result of a detailed trade-off analysis considering several criteria such as accuracy, computational complexity, possible numerical issues, flexibility for further future upgrades (i.e modularity of the architecture) as well as theoretical results on optimality of the solution. However, the following set of constraints was assumed to feed the trade-off and design phases.

- The Absolute Navigation System consists of a Star Tracker, an Inertial Measurement Unit (IMU), a Global Navigation Satellite System (GNSS) receiver and a sensor fusion algorithm.
- The IMU is a tactical grade MEMS unit with an update rate of 100Hz. The Absolute Navigation filter will include the estimation of the IMU measurement biases assuming all the other systematic sources of errors (i.e. mutual and installation misalignment, temperature variations cross-coupling effects, non-linearity and so on) already compensated or negligible. This assumption could be summarized considering the following IMU measurement model:

$$\begin{bmatrix} \omega_m \\ a_m \end{bmatrix} = \begin{bmatrix} \omega_t + \omega_b \\ a_t + a_b \end{bmatrix} + \begin{bmatrix} \eta_\omega \\ \eta_a \end{bmatrix} \quad (1)$$

  where:
  - ω_m and a_m are the gyro and accelerometer measurements respectively
  - ω_t and a_t are the true angular velocity and acceleration respectively
  - ω_b and a_b are the gyro and accelerometer biases respectively
  - η_ω and η_a are the gyro and accelerometer noise respectively
- The Star sensor provides the unbiased true attitude plus a noise term that will include all the Star sensor measurement errors; the update rate is 5Hz
- The GNSS receiver is a multi-constellation, single-frequency receiver with 30 channels and an update rate of 1Hz. The systematic and known errors (i.e relativity errors) of receiver's output (pseudoranges and pseudorange rates) are already corrected by using for example a tight integration scheme. Furthermore, the GNSS receiver also provides the ephemeris information (or equivalently the best received-satellite positions and velocities computed from the ephemeris file).
- Considering the application segment and the related required accuracy performance, the gravitational model used in the absolute navigation filter equations assumes a homogenous spherical Earth and more precisely it considers the most significant or largest spherical harmonic term, which accounts for the Earth oblateness (i.e J2 term).

Moreover, in case of unpowered flight, it is considered that the non-gravitational perturbations are essentially due to the atmospheric drag (especially for low orbits), which rapidly decreases for higher orbits, albedo, and Solar pressure that becomes the uppermost for GEO and higher orbits [12].

The architecture selected after the abovementioned trade-off analysis consists in a single (centralized) Square-Root Unscented Kalman Filter [13] running at the maximum available measurement rate (100Hz). The standard UKF is a nonlinear filtering technique based on the concept of Unscented Transformation (UT), a formal mathematical method for propagating a probability distribution through a nonlinear transformation. In more details, the UT allows estimating the output mean and

covariance of a nonlinear function by computing the weighted mean and covariance of a discrete set of points (named sigma points) deterministically chosen in the domain of the function. Using this method, the UKF provides at least second-order accurate evaluations of the first two statistical moments of the unknowns, enabling a complete and structured statistical characterization of the estimated variables and leading to a reliable evaluation of the uncertainties on the estimations. Nevertheless, like all Kalman filters, the UKF performs the estimation in two sequential phases. First, a dynamic model, whose state vector is composed of the unknowns, is used for time propagation of the estimation (prediction phase). Then, at each time step, the available measurements are compared with the prediction (that is, the dynamic model outputs) to refine the estimation (correction phase). Furthermore, to mitigate the effects of well-known numerical issues of an unscented Kalman filter implementation (i.e. possibility of numerical instability, positive semi-definitiveness of the state covariance to apply Cholesky decomposition and so on), a SR-UKF formulation has been preferred for the presented application.

Concerning the orbital filer model, an Earth Centred Integration (ECI) reference frame was assumed, with unity vectors given by $\hat{x}, \hat{y}, \hat{z}$. A classical Cartesian formulation of the motion equations and attitude kinematics is:

$$\dot{p} = v \tag{2}$$

$$\dot{v} = a_{ng} + a_g \tag{3}$$

$$\dot{q} = \frac{1}{2}\Omega(\omega) \tag{4}$$

Where $p = [x, y, z]^T$ and v are respectively the position and velocity of the VINAG system in the ECI reference frame and q is the quaternion representing the VINAG system attitude with respect to the ECI frame. The matrix $\Omega(\omega)$ is the skew matrix function of the angular velocity $\omega = \left[\omega_x, \omega_y, \omega_z\right]^T$.

$$\Omega(\omega) = \begin{bmatrix} 0 & -\omega_x & -\omega_y & -\omega_z \\ \omega_x & 0 & \omega_z & -\omega_y \\ \omega_y & -\omega_z & 0 & \omega_x \\ \omega_z & \omega_y & -\omega_x & 0 \end{bmatrix} \tag{5}$$

The acceleration a_{ng} represents the total non-gravitational acceleration, sum of solar pressure, aerodynamic friction, and other perturbations, while a_g is the gravitational acceleration approximated to the 2nd order term and given by [14]:

$$a_g = -\frac{GM}{|p|^3}\begin{bmatrix} x - \frac{3x}{2}J_2\left(\frac{R_e}{|p|}\right)^2\left(5\frac{z^2}{|p|^2} - 1\right) \\ y - \frac{3y}{2}J_2\left(\frac{R_e}{|p|}\right)^2\left(5\frac{z^2}{|p|^2} - 1\right) \\ z - \frac{3z}{2}J_2\left(\frac{R_e}{|p|}\right)^2\left(5\frac{z^2}{|p|^2} - 3\right) \end{bmatrix} \tag{6}$$

Where GM is the product of the universal gravity constant and the Earth mass (that in the WGS84 system is equal to 3.9860050e14 m^3/s^2), R_e is the equatorial Earth radius (6378137 m) and J_2 is the 2nd degree harmonic coefficient.

In addition, some Gauss-Markov processes model the non-gravitational acceleration, the gyro bias ω_b, the GNSS receiver time delay δt and related drift k_t as reported below:

$$\dot{a_{ng}} = \eta_{ng} \tag{7}$$

$$\dot{\omega_b} = \eta_{\omega} \tag{8}$$

$$\dot{\delta t} = k_t + \eta_{\delta t} \tag{9}$$

$$\dot{k_t} = \eta_{k_t} \tag{10}$$

where η_{ng}, η_{ω}, $\eta_{\delta t}$ and η_{k_t} are the respective zero mean white Gaussian noise processes.

Based on Eq. (2-10), the total number of the process states is 18, but using a minimal attitude representation based on the Rodrigues Parameters [15], allows reducing the total internal filter state dimension to 17.

Thanks to the specific SR-UKF architecture, the filter is able to cope with a variable number of measurement available step by step, simply propagating and correcting the covariance matrix (and the estimated state) using only the available measurements.

In order to perform the model propagation phase, equations (2), (3), (7)-(10) are discretized using a 1th and/or 2nd order Taylor series approximation, while equation (4) is discretized adopting a standard literature quaternion propagation/integration equation [16].

For what concern the correction phase, but also for sigma-points definition and propagation, covariance matrix estimation and so on, SR-UKF approach requires different algebraic operations on the estimated state. For example, the correction to the current propagated state is added and averaged after the sigma-point propagation. Precisely, while state elements other than quaternions (or Rodrigues parameters) are defined in a Cartesian space allowing normal algebraic manipulation, the quaternion statistical propagation needs a special care, because a normal weighted arithmetic average of sigma points yields to a non-unit quaternion estimate [17]. To this end, a specific algorithm proposed in [18] has been used that allows averaging on a unit hypersphere manifold in order to obtain a unit-norm reference optimal quaternion.

The measurements of the orbital filter in this study include: i) up to 30 pseudoranges and 30 pseudorange rate measurement from GNSS receiver related to the current visible satellites, ii) attitude measurement from Star sensor, iii) angular velocities from the gyroscopes, iv) acceleration measurements from accelerometers used only when VINAG system is subject to manoeuvring conditions. In this case, the accelerometer bias is neglected. Finally, in order to obtain a more accurate position estimation, also a dedicated masking algorithm was implemented in case of GEO (or higher) orbits. Specifically, low elevation satellites' measurements were not included in the filter, considering that for these satellites, the measurement error can be strongly auto-correlated (and however in presence of satellite signals which intercept ionosphere) due to relevant atmospheric delays [19].

3.2 Relative Navigation

The absolute state of the spacecraft, obtained by the absolute navigation filter, are the input of the relative navigation filter block. The relative state determination algorithm is composed by two main, strongly interconnected blocks.

A general scheme of the architecture is depicted in Figure 2. The relative pose $\boldsymbol{t}$,R (being $\boldsymbol{t}$ the translation vector and R the rotation matrix) is estimated by the Monocular Pose Determination block and then fed to the filtering block, which is composed of two sections for translational and rotational dynamics, respectively. The relative state estimate provided by these filters is provided in feedback to the pose determination block each time a new image is available.

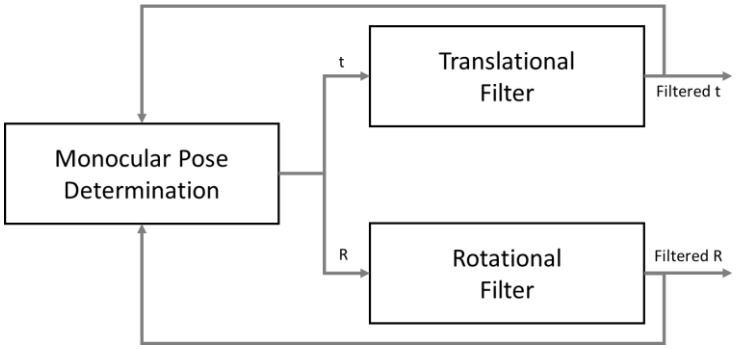

Figure 2. Relative Navigation Architecture.

Vision-based relative navigation filter

A decoupled architecture is chosen for the navigation filter. In fact, by neglecting external disturbances and spacecraft flexibility, the relative translational and rotational dynamics are decoupled.

Translational filter

For the translational part of the filter, an H-∞ Filter is selected. The standard Kalman filter is the optimal estimator for linear systems with zero-mean Gaussian process and measurement noise. However, if these assumptions do not hold, robust filtering techniques can outperform the Kalman filter. This kind of filter is called H-∞ filter or also minimax filter. It minimizes the ∞-norm of the estimation error and it does not make any assumptions about the statistics of the process and measurement noise [20].

In the considered case, the measurements are the output of the pose estimation block, i.e. the relative position between the two centers of mass. The formulation of the H-∞ Filter constrains the choice to linear relative dynamics model. For this reason, in this work, the authors used the formulation by Yamanaka and Ankersen [21] as filter dynamical model. In the cited paper, they developed a linearized formulation for arbitrary elliptical orbits. Moreover, the derived state transition matrix representation is advantageous in the implementation of filtering techniques.

Rotational filter

For the rotation part, a second-order minimum energy filter on the Lie group is implemented. The use of a minimum energy filter on SO(3) is justified by the fact that, thanks to the Lie group structure of SO(3), this class of filters is shown to outperform the classical Multiplicative Extended Kalman Filter [22].

In this paper, a modification to the second-order minimum energy filter proposed by Saccon [23] is introduced without considering the dynamics of the system. In particular, the filter is adapted to be used in a relative scenario and without the knowledge of the exact inertia properties of the target.

The complete formulation of the second-order filter without the dynamics terms is outlined in Table 1, where R is the relative rotation matrix, ω is the relative angular velocity vector, K is the filter gain, r^R and r^ω are the filter residuals. For the complete derivation of the filter, please refer to [23].

Table 1. Second-order minimum energy filter.

Initialization:

$$\hat{R}(t_0) = \hat{R}_0, \hat{\boldsymbol{\omega}}(t_0) = \hat{\boldsymbol{\omega}}_0,\ K(t_0) = K_0,$$

Filtering:

$$\dot{\hat{R}} = \hat{R}\left(\hat{\boldsymbol{\omega}}(t) + K_{11}\boldsymbol{r}^R + K_{12}\boldsymbol{r}^\omega\right)_\times,$$

$$\dot{\hat{\boldsymbol{\omega}}} = K_{21}\boldsymbol{r}^R + K_{22}\boldsymbol{r}^\omega,$$

$$\dot{K}(t) = -\alpha K + AK + KA^T - KEK + BR^{-1}B^T - WK - KW^T,$$

where

$$\boldsymbol{r}_t = \begin{bmatrix} \boldsymbol{r}^R \\ \boldsymbol{r}^\omega \end{bmatrix} = \begin{bmatrix} -\boldsymbol{u}_1(\hat{\boldsymbol{r}}_1 \times \boldsymbol{r}_1) - \boldsymbol{u}_2(\hat{\boldsymbol{r}}_2 \times \boldsymbol{r}_2) \\ \mathbf{0} \end{bmatrix},$$

$$u_i = \frac{b^2}{d_i^2},$$

$$\hat{\boldsymbol{r}}_i = \hat{R}^T\bar{\boldsymbol{r}}_i, \quad \boldsymbol{r}_i = \hat{R}^T\bar{\boldsymbol{r}}_i + d_i\boldsymbol{\epsilon},$$

$$A = \begin{bmatrix} -\hat{\boldsymbol{\omega}}_\times & I \\ 0 & 0 \end{bmatrix},$$

$$E = \begin{bmatrix} \sum_{i=1}^{2} \boldsymbol{u}_i\left((\hat{\boldsymbol{r}}_i)_\times(\boldsymbol{r}_i)_\times + (\boldsymbol{r}_i)_\times(\hat{\boldsymbol{r}}_i)_\times\right)/2 & 0 \\ 0 & 0 \end{bmatrix},$$

$$BR^{-1}B^T = \begin{bmatrix} 0_{3\times3} & 0 \\ 0 & BR^{-1}B^T \end{bmatrix}$$

$$W = \begin{bmatrix} \frac{1}{2}\left(K_{11}\boldsymbol{r}^R + +K_{12}\boldsymbol{r}^\omega\right)_\times & 0 \\ 0 & 0 \end{bmatrix}.$$

Monocular pose determination

The pose determination block (see Figure 1) is a critical component of the architecture designed for relative navigation toward a non-cooperative target based on the monocular camera system of VINAG. This block includes the implementation of all the techniques and algorithms required to estimate the relative position and attitude of the target with respect to the camera (pose) by processing raw sensor data (i.e., 2D images). In this respect, it is worth to outline that the pose determination block foresees two distinct steps, i.e., acquisition and tracking. Pose acquisition is carried out as soon as the first image, acquired by the monocular camera system, is available. Consequently, no a-priori information about the relative position and attitude of the target can be exploited to aid the processing operations. Once successful pose acquisition is confirmed, the tracking phase can be started, during

which the pose parameters are updated (at higher frequency) taking advantage of the navigation information at the previous time instants provided by the navigation filter. Considering the mission scenarios of interest to VINAG, it is possible to state that the uncooperative target is a known space object, i.e., at least a simplified model of its geometry is available, and it can be stored on board. Consequently, pose determination is entrusted to model-based algorithms which are designed to look for an optimal match between natural features (e.g. corner or edges), extracted from the acquired images, and the target model. These model-based approaches require three online steps, as shown in Figure 3.

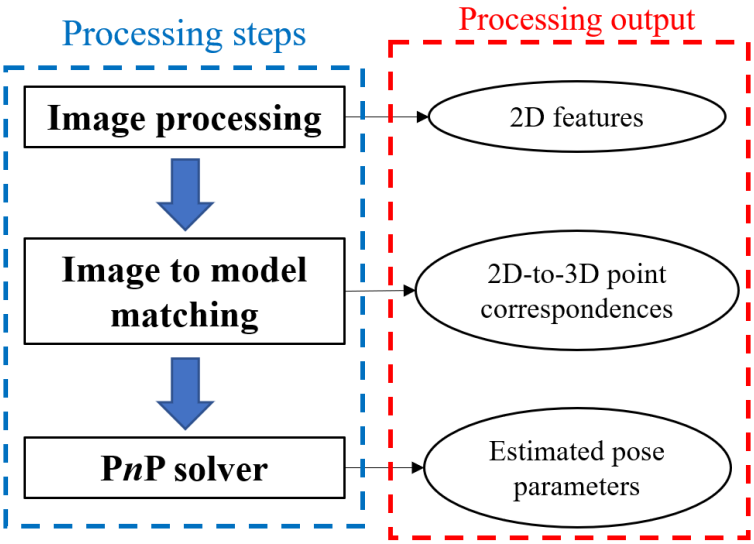

Figure 3. Monocular model-based algorithms: processing steps and output.

Image processing is needed to extract from the acquired image a set of 2D features, which are representative of the target appearance in the camera Field-of-View (FOV). Image to model matching is aimed at finding correspondences between these features and the elements of a dataset of similar objects obtained from the target model. Finally, once a set of correspondences is available, the pose parameters are estimated by implementing a proper solver for the Perspective-n-Point (PnP) problem. The specific solutions adopted in VINAG for each of these steps, considering both the acquisition and tracking phases, are now presented in detail. Concerning image processing, the same technique is adopted for both pose acquisition and tracking. Corners have been selected since the associated detectors (e.g., Harris [25], Shi-Tomasi [26]) are characterized by much lower computational burden than the one required by more complex feature descriptors (e.g., SIFT [27]). Hence, they are suitable for real-time implementation even when limited processing resources are available (which is the case for small satellites applications). Once a set of 2D corners has been extracted from the acquired image, they must be matched to a set of 3D landmarks, i.e., the target model, which is built offline from the knowledge of the target geometry. These landmarks are basically the real 3D corners of the target which are highly likely to be extracted by the corner detector. An example of target model in which the 3D landmarks are highlighted is shown in Figure 4.

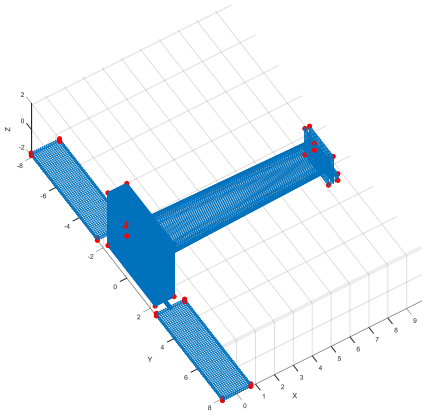

Figure 4. 3D landmarks (red circles) composing the simplified model of a potential target (XMM-Newton).

The remaining processing steps identified in Figure 3 are coupled, meaning that the problem of finding correct 2D-3D point correspondences and the subsequent estimation of the pose parameters (PnP solution) must be dealt with simultaneously. Two distinct ad-hoc solutions have been selected and implemented for acquisition and tracking, respectively.

With regards to pose acquisition, an original approach is presented. It is based on a customized implementation of the Random Sample Consensus method (RANSAC) [28] to carry out image-model matching, while it uses the Efficient Perspective-n-Points (EPnP) algorithm [29] as PnP solver. RANSAC is a hypothesize-and-test approach meaning that it iteratively generates a set of 2D-3D matches by gradually enlarging a relatively small "consensus set", i.e., a set of hypothesized point-to-point correspondences. At each iteration, the test consists of applying the selected PnP solver to the consensus set to verify the correctness of the correspondences. Once the initial consensus set, S_1, is created, a tentative pose solution provided by the PnP solver is used to project the 3D landmarks on the image plane using the classical equation of the perspective projection based on the pinhole camera model, as shown hereunder.

$$\boldsymbol{P}^r = f \begin{bmatrix} \frac{P_x^c}{P_z^c} \\ \frac{P_y^c}{P_z^c} \end{bmatrix} \tag{11}$$

Where f is the camera focal length, while $\boldsymbol{P}^C = (P_x{}^C\, P_y{}^C\, P_z{}^C)$ is a generic 3D landmark converted from the Target Reference Frame (T) to the Camera Reference Frame (C) using the equation below.

$$\boldsymbol{P}^c = R_{TC}\boldsymbol{P} + \boldsymbol{t} \tag{12}$$

And where R_{TC} and $\boldsymbol{t}$ are the relative rotation matrix and position vector, respectively, provided by the PnP solver. At this point, the corners extracted from the image and the 3D landmarks of the model re-projected on the focal plane are processed by a feature-matching algorithm which aims at enlarging the consensus set. Specifically, each of the re-projected corners is tentatively associated to the image feature which provides the minimum distance. If the Euclidean distance falls below a threshold, the image-model correspondence is confirmed. The output of this process is an enlarged consensus set S_1*. If the number of 2D-3D matches stored in S_1* reaches a pre-defined value (correspondence

condition), the algorithm is terminated. Otherwise, a new random consensus set (S_2) must be defined and the whole procedure has to be repeated. This standard RANSAC implementation is customized by exploiting heuristics, i.e., the knowledge of the target shape, to accelerate the search for 2D-to-3D corner matches (so that is not based on purely random image-model associations). Indeed, the main drawback of RANSAC-based approaches is the significant computational load arising from the fact that S1 is chosen randomly. Consequently, an ad-hoc strategy has been conceived which exploits the knowledge of the target geometry. In details, S1 is built by considering only a limited number of 3D landmarks, i.e. those belonging to spacecraft components which are clearly separated with respect to the target center of mass (e.g., solar arrays, telescopes, antennas). This approach derives from the fact that if the target is fully visible in the camera FOV, the probability that the above-mentioned elements are far from the image centroid on the focal plane is extremely high. Clearly, the restricted set of 3D landmarks is selected off-line, depending on the target under consideration. On the other hand, the 2D corners extracted from the image are classified exploiting an image processing strategy which is based on the potential of the Principal Component Analysis (PCA) [30]. The PCA is a technique used to analyze multidimensional datasets. Specifically, it aims at deriving their principal directions, i.e. the main related information, by studying eigenvectors and eigenvalues of the associated covariance matrix. So, when applied to the set of 2D corners extracted from the image, PCA allows classifying them into different sub-sets depending on their distribution with respect to the image centroid. Once, this classification is accomplished, it is possible to significantly restrain the computational time by searching for 2D-3D correspondences considering only these restricted sub-sets of 2D and 3D corners.

With regards to the tracking step, the SoftPOSIT algorithm [31] has been selected due to its capability to simultaneously ensure adequate levels of accuracy and update rate. This method integrates an iterative pose determination technique (POSIT, i.e., Pose from Orthography and Scaling with ITerations) and an iterative correspondence assignment approach (Softassign), into a single operation loop. Specifically, unlike EPnP which provides a closed-form solution to estimate the pose parameters, the PnP solution provided by softPOSIT is a non-linear optimization of a purposely defined cost-function [31].

5. HARDWARE DESIGN

In this section, an overview of the hardware design of VINAG is provided.

4.1 VINAG Central Unit

Vision-based Navigation & Data Fusion and VISNAV HW acceleration modules

The VISion based Navigation (VISNAV) & Data Fusion Module (VDFM) is the core of VINAG Central Unit; it takes care of the video data acquisition from the Camera System, the image data processing and the monocular pose determination, the reception of the data coming from the GNSS receiver and the IMU and finally the implementation of the navigation data fusion algorithms. The VDFM is based on a Microsemi RTG4 Flash FPGA, whose large logical resources are mainly dedicated to the HW implementation of the algorithms, or parts of them, requiring intensive-computing; in the same RTG4 FPGA is also implemented a SW IP core Processor that is employed for the control of the entire VINAG system and to run algorithms or the high level of them, involving a computational load compatible with a SW implementation. For the execution, at the required rate, of the VISNAV algorithms, representing the most demanding computational load, the VDFM can

dispose (when needed) of an HW Acceleration Module that is based on two XQR5VFX130 Xilinx FPGAs; thanks to a larger amount of internal memory (w.r.t. the Microsemi RTG4), that Xilinx's RAM based FPGA is able to reach typically higher rate, when implementing image processing algorithms. It presents, as drawback, a higher power consumption, but, being used as accelerator, it is not always active or it is at low duty cycles. Data transfer between the VDFM and the HW Acceleration Module is carried out at very high data rate (up to 1.575Gbit/s) by means of two Channel Link SerDes, working in opposite directions.

IMU

The Inertial Measurement Unit (IMU) for the VINAG system is a MEMS based equipment, which has been considered the best compromise between SWaP (Size, Weight and Power) requirements and sensor's accuracy. Specifically, the state-of-the-art (ITAR free) MEMS technology for this unit's class currently allows having a bias stability on the order of 0.1deg/hr for gyroscopes and 0.015mg for accelerometers that has deemed to be sufficient for the applications of interest, as it will be also shown in the following sections.

GNSS receiver

The Space Borne GNSS Receiver developed by Space Technology is based on a single ZynQ FPGA device capable of acquiring and tracking Multi-constellation GALILEO L1 and GPS L1 C/A signals. It is the first European GNSS Receiver in single FPGA, or single ASIC form, integrating in a single digital chip both a Fast Acquisition Unit (FAU) and a GNSS Tracker up to six PRNs. In VINAG, the FAU and Tracking engine are used to estimate the Pseudo Range and the Doppler observables further processed by the filter described in Section 3.1. The GNSS Receiver characteristics and measured Tracking and Acquisition performances can be summarized in Table 2.

Table 2. Space Technology LEO GNSS Receiver characteristics and tested performances

GNSS Receiver Char.	**Value**	**GNSS Receiver Char.**	**Value**
Doppler Excursion	+/-60KHz	Doppler rates	+/-620Hz/sec
Supported Constellation	GPS L1 C/A and GALILEO L1C/L1B	Number of Correlator Channels	>= 6
Acquisition Threshold @+/-60KHz	37dB-Hz	Acquisition Threshold @+/-40KHz	35dB-Hz
GPS L1 C/A single PRN Acquisition time	40 ms	GALILEO L1 single PRN Acquisition time	95 ms
Cold Start worst case TTFF	50.5 sec.	Warm Start worst case TTFF	9 sec.

4.2 Cameras System

Monocular camera for pose estimation

The VINAG Camera System is composed by two CMOS Monocular cameras and one Star Sensor. The CMOS Monocular camera is a very compact, low power and high performance CMOS Camera, specifically designed, by TSD, for space applications on board small platforms. The camera is based on a Microsemi RT3PE3000L Flash FPGA and a Focal Plane Assembly, that hosts a CMOS APS sensor, acquiring color images, with a frame rate up to @30fps and two possible formats: 1920x1080(1080p) and 1280x720 (720p). The image acquisition can be synchronized with an external trigger or a self-generated internal one. The CMOS Monocular camera is provided with a CAN bus interface for the camera configuration & control and a Channel Link Serializer for the image data transmission to the VDFM at 1.2Gbit/s. The camera adopts a very rugged, conduction cooled,

thermal- structural design and it is equipped with ±50° FOV lens. A more detailed description of this camera can be found in [32].

Star sensor

A compact Star sensor suitable for micro- and nano-satellites has been considered for VINAG, characterized by low power consumption (< 1W), low mass (< 1kg), an output rate of 5 Hz and sufficient attitude determination accuracy (a bore-sight accuracy of 2.5 arcsec and a roll axis accuracy of 5 arcsec).

6. SIMULATED PERFORMANCE

The algorithms described in Section 4, were tested and validated preliminarily by carrying out numerical simulations, adopting simplified parametric models of the observations. In the next step of our project, realistic hardware-in-the-loop tests will be performed to validate the hardware implementation as well as both its absolute and the relative navigation capabilities. The following sections describe the models and assumptions adopted in the simulations and the obtained results.

5.1 Models and assumptions

In the following, the reference scenarios, the model of each observation considered in our simulations are detailed. Note that the assumptions of this analysis are not completely representative of the GNSS receiver described in Section 4.1 of Space Technology S.r.l., which in this first step of the project is only suitable for LEO.

GNSS observations

The GPS L1 C/A and Galileo E1 signals were assumed to be transmitted by up to 30 GPS and 30 Galileo satellites, by modelling their realistic power level at the receiver position, taking into account 3D receiver and transmitters antenna pattern. A receiver sensitivity of 35 dB-Hz was assumed in LEO, while of 28 dB-Hz in GEO. Pseudorange observables are affected by systematic and non-systematic errors that can be classified into: satellite clock error and broadcast satellite ephemeris error, atmospheric delay, multipath effect and receiver error. According to [33], these errors can be assumed as white Gaussian noise with a certain standard deviation (although this is not strictly true, it is sufficient for the purpose of this study). The overall error that affects pseudoranges can therefore be described by the user equivalent range error (σ_{UERE}), defined as the root sum square of the different range error contributions. Table 3 reports the ones assumed in our simulations. In particular, residual of broadcast clock and ephemeris as well as multipath (generated by the spacecraft surfaces) were modelled according to the values proposed in [33]. While no signal crossing the troposphere is considered in the navigation solution, a standard deviation of 10 m was assumed as residual noise due to the ionospheric delay only in LEO (when the receiver is orbiting below the upper bound of the ionosphere and then, when the received signals cross the ionosphere). In GEO instead, no atmospheric delay is taken into account since the few signals crossing the atmosphere are simply discarded. The receiver error was modelled as function of the receiver characteristics and of the carrier-to-noise-ratio C/N_0, according to the formulation (5.23) of [33].

Table 3. Assumed user equivalent range error contributions.

Error source	$\mathbf{1\sigma\ error\ (m)}$
Broadcast clock	1.1
Broadcast ephemeris	0.8
Ionospheric delay	$10\ if\ h < 1000\ km$
Receiver error	$f(C/N_0, receiver\ parameters)$
Multipath	0.2

IMU and Star sensor observations

The IMU and Star sensor observations were modelled according to the description already provided respectively in Section 3.1 and 4.2.

Monocular camera observations

In this step of the project, since our purpose was only to validate the vision-based pose determination algorithms described in Section 3.2, in our simulations for each acquired image, we directly modelled the extracted features on the image frame, corresponding to each considered relative state of the camera with respect to the assumed orbiting target, without modelling instead the image acquisition and features extraction processes.

5.2 Simulation Results

Absolute navigation performance

The absolute navigation performance was preliminary evaluated by means of simulations in a LEO and GEO scenario. Simulation scenarios were defined using a high fidelity simulation tool developed by PoliMi, including non-uniform mass distribution of the Earth, solar radiation pressure, atmospheric drag, third body perturbation (sun and moon), gravity gradient and magnetic field perturbation. The PoliMi high fidelity astrodynamic tool has been developed to support the Mission Analysis and Design for different financed studies such as PlAtiNO and CHRISTMAS (ASI supported) and S3Net (H2020 framework study).

Precisely, in LEO as reference, we assumed the THAS-I Nimbus platform characterized by a class cubic shape, size of [0.8, 0.8, 1.6] m, drag coefficient equal to 2.2 degrees and mass of 100 kg. The Keplerian orbital parameters of the reference initial orbit are: semi-major axis of 7158 km, eccentricity null, inclination of 98,5 degrees.

In GEO we investigate the VINAG system capabilities in an orbit well above the GNSS constellations. The reference platform is the THAS-I PRIMA. In this case the Keplerian orbital parameters are: pericenter height of 36000 km, eccentricity and inclination both null.

The data generated by the high fidelity simulation tool to model the reference orbit (representing the "true" one), were processed by using a set of dedicated avionic sensor simulators (i.e IMU, GNSS receiver and Star sensor) according to the above defined items. The sensor outputs fed the Absolute Navigation filter providing the full state estimation.

Furthermore, simulations were carried out also including 300ms and 6μs/s of respectively receiver clock's bias and drift with the respect to both GPS and Galileo transmitters' clock.

Figure 5 and Figure 6 display respectively the positioning and attitude determination errors in the considered LEO scenario. Similarly, Figure 7 and Figure 8 show the same errors in the considered GEO scenario. In LEO, the positioning error has a standard deviation lower than 3 m on all the axes, while in GEO smaller than 6 m on x- and y- axes, and smaller than 1 m on z- axis. A poorer accuracy in GEO is expected by accounting for the worsening of the receiver/transmitters relative geometry, known as Geometric Dilution Of Precision (GDOP) and also for an higher receiver noise due to lower C/N_0 levels. The attitude estimation is always quite accurate with an error smaller than 0.06°in LEO and in GEO (except for a higher initial peak).

Furthermore, Figure 9 and Figure 10 show the number of total satellites effectively used with respect to the visible ones as result of the masking algorithm described above. As expected in GEO, due to

highest probability of signals coming from the weaker side lobes of the transmitters' antenna, the average availability is lower than in LEO.

The estimation accuracy obtained demonstrates the effectiveness of VINAG absolute navigation algorithm, in different scenarios (LEO and GEO). Further improvements are currently under investigation related to a GEO adaptive Kalman Filter tuning algorithm taking into account the received satellites signal-to-noise ratio (as done in [34]), as well as possible masking in order to avoid noisy pseudorange measurements.

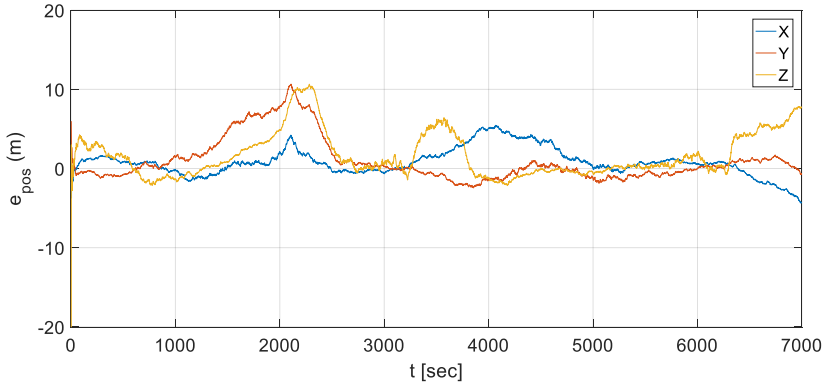

Figure 5. Positioning error in the considered LEO.

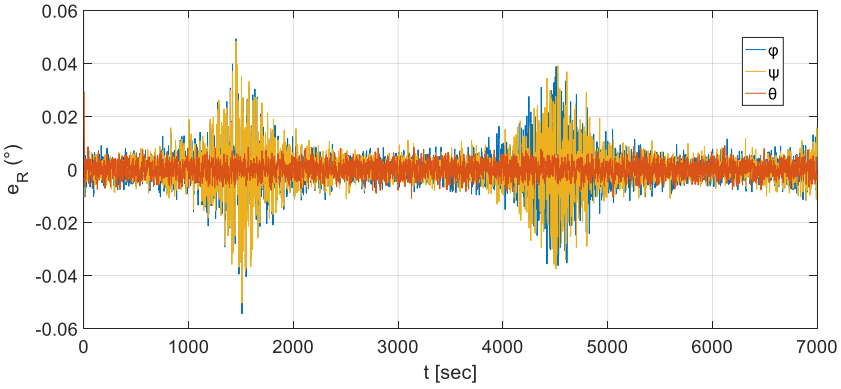

Figure 6. Attitude determination error in the considered LEO.

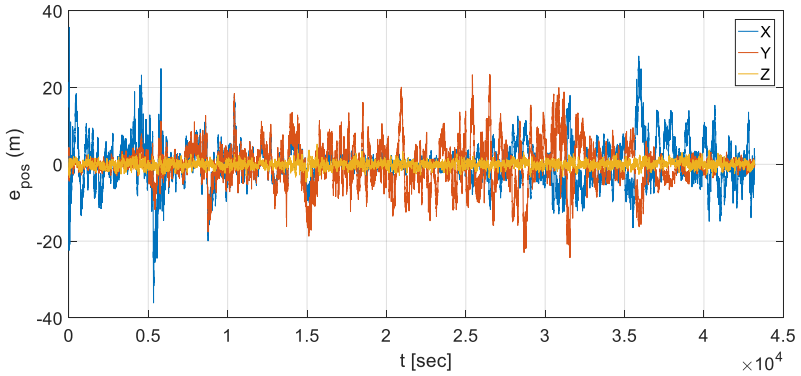

Figure 7. Positioning error in the considered GEO.

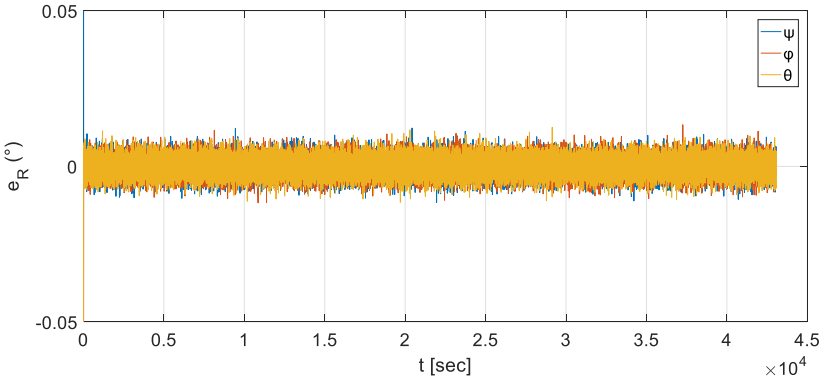

Figure 8. Attitude determination error in the considered GEO.

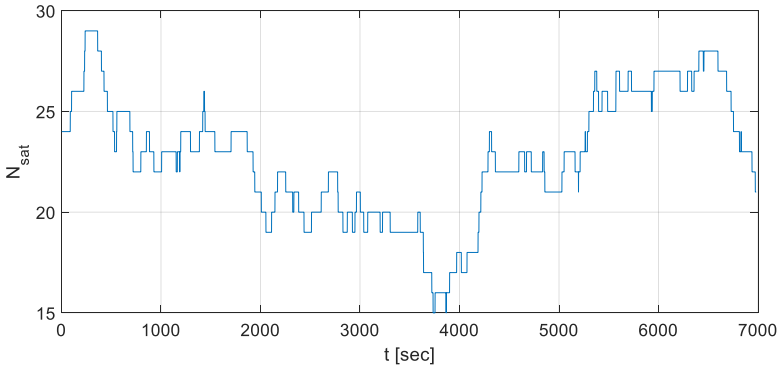

Figure 9. Number of available GNSS satellites in the considered LEO.

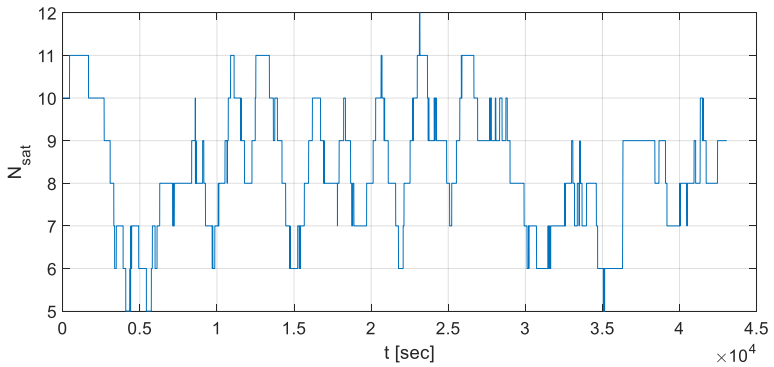

Figure 10. Number of available GNSS satellites in the considered GEO.

Relative navigation performance

The relative navigation filter is tested in the aforementioned LEO scenario. The assumed initial relative conditions are $\rho_0 = [0, 30, 0]\, m$ for the position and $\dot{\rho}_0 = [0, -1, 0] * 10^{-4}\, m/s$ for the relative velocity, expressed in the local-vertical, local-horizontal (LVLH) reference frame fixed to the chaser spacecraft center of mass. For the relative dynamics, a torque-free motion has been imposed to the simulated target spacecraft. The motion has been simulated using the classical Euler equation for rigid body, imposing the following initial conditions: $\omega_T = [1, 0, 0] deg/s$. To preliminary assess the performance of the proposed approaches for monocular pose determination, as mentioned in Section 5.1, simulated images of the target are generated by projecting the actual 3D corners composing a simplified model of the target on the image plane. Potential errors caused by image processing are considered by modifying the ideal position of each corner on the image plane by adding to its horizontal and vertical coordinates a random Gaussian noise, whose standard deviation (σ_{pix}) is expressed in terms of a certain number of pixel. Moreover, a number of false corners (n_{out}) is randomly located in the region of the image plane occupied by the target (according to a uniform distribution) to simulate the presence of outliers in the measurements provided by the image processing. Both pose determination and filtering block are assumed to work at 1Hz. To assess the pose estimation performance, the following estimation errors are defined: $e_\rho = \sqrt{(x_i - \hat{x}_i)^2 + \left(y_i - \hat{y}_i\right)^2 + (z_i - \hat{z}_i)^2}$ is the position error, where $\hat{x}_i$, $\hat{y}_i$, $\hat{z}_i$ are the position components estimates and x_i, y_i, z_i are the true position components, obtained by integrating the complete nonlinear differential equations of the unperturbed relative motion. Similarly, the velocity error is $e_{\dot{\rho}} = \sqrt{\left(\dot{x}_i - \hat{\dot{x}}_i\right)^2 + \left(\dot{y}_i - \hat{\dot{y}}_i\right)^2 + \left(\dot{z}_i - \hat{\dot{z}}_i\right)^2}$. Finally, the relative attitude error is computed as $e_R = \text{acos}\left(1 - \frac{tr\left(I - R_i^T \hat{R}_i\right)}{2}\right)$, with $\hat{R}_i$ being the estimated rotation matrix at time *i*.

In Figure 11, the numerical simulation results of the relative position error are illustrated. The error of the pose determination block alone and coupled with the filter are shown.

Similarly, the performance of the second-order minimum energy filter were analyzed and in Figure 12, the global relative attitude error and for each single axis are reported. Also in this case, the presence of the filter improves the accuracy of the relative attitude estimation. The error angle is always below 3 degrees.

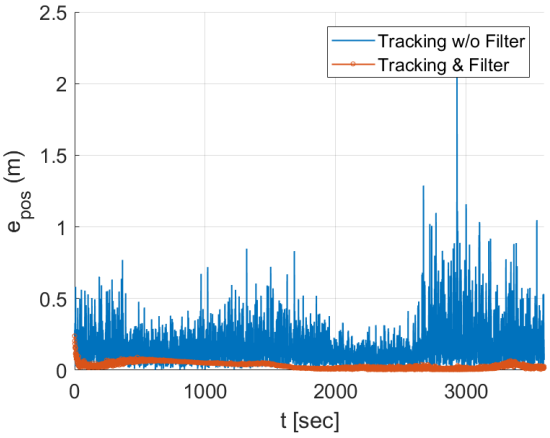

Figure 11. Relative Position Error.

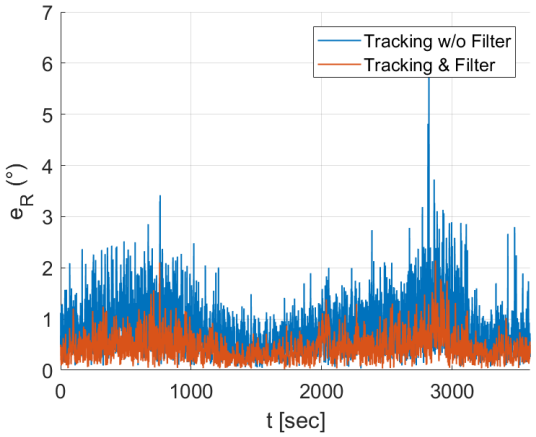

Figure 12. Relative Attitude Error.

7. CONCLUSIONS

In this paper we introduced the system VINAG, currently under development by a team of Italian companies and universities, co-financed by the Italian Space Agency. VINAG has been specifically designed to provide on board, autonomous absolute and relative spacecraft navigation. In particular, in this study, we provided a detailed description of the navigation algorithms of VINAG, implemented for orbit and attitude determination as well as for vision-based pose estimation of an orbiting non-cooperative target. In a first step of our project we carried out preliminary simulations to validate the sensor fusion architecture and the implementation of all the adopted algorithms. The obtained results of the achievable navigation performance here reported, assessed the correctness of the implementation. In addition, a short overview of the hardware design was also given. In a second and final step of the project, following the completion of the hardware implementation and of the overall system development, the complete capabilities of VINAG will be also validated by means of hardware-in-the-loop tests.

8. REFERENCES

[1]. IPC-THAG, AOCS SENSORS and Actuators II Specific Sensors and Actuators (INCL IMU), ESA/IPC/THAG(2015)7

[2]. B. Polle, B. Frapard, et al. "Robust INS/GPS Hybrid Navigator Demonstrator Design for Launch, Re-entry and Orbital Vehicles". In: 7th International ESA Conference on Guidance, Navigation and Control Systems, 2008.

[3]. M. Giannini, M. Melara, C. Roux, ALTS localization system of vega launcher: vv02 post-flight analysis & gps issues for future hybrid navigation, 9th International ESA Conference on Guidance, Navigation & Control Systems, 2014, Porto, Portugal.

[4]. Honeywell, E-SIGI Enhanced Space Integrated GPS/INS, 2004. https://aerocontent.honeywell.com/aero/common/documents/myaerospacecatalog-documents/Space_Integrated_GPS-INS.pdf

[5]. V. Capuano, E. Shehaj, P. Blunt, C. Botteron, P.-A. Farine. High accuracy GNSS based navigation in GEO. Acta Astronautica, Volume 136, July 2017, Pages 332–341, http://dx.doi.org/10.1016/j.actaastro.2017.03.014

[6]. V. Capuano, C. Botteron, J. Leclere, J. Tian, Y. Wang and P.-A. Farine. Feasibility study of GNSS as navigation system to reach the Moon, in Acta Astronautica, vol. 116, p. 186-201, 2015. http://www.sciencedirect.com/science/article/pii/S0094576515002520

[7]. V. Capuano, P. Blunt, C. Botteron, J. Tian, J. Leclère, Y. Wang and P.-A. Farine. Standalone GPS L1 C/A Receiver for Lunar Missions, in Sensors, vol. 16, num. 3, p. 347, 2016. http://www.mdpi.com/1424-8220/16/3/347

[8]. J. Miller, Tokyo, Japan, Enabling a Fully Interoperable GNSS Space Service Volume, 6th International Committee on GNSS (ICG), 2011, Tokyo, Japan.

[9]. G. Flandin , B. Polle, J. Lheritier and P. Vidal, Vision based navigation for autonomous space exploration, NASA/ESA Conference on Adaptive Hardware and Systems (AHS), 15-18 June 2010, Anaheim, CA, USA, doi: 10.1109/AHS.2010.5546273

[10]. Navigation for Planetary Approach & Landing – FINAL REPORT, ESA Contract Reference 15618/01/NL/FM – May 2006

[11]. C. Kaiser et alii, Vibanass Test Results and Impacts on Kayser-Threde Active Debris Removal Strategy, Proceedings of 64th International Astronautical Congress, 23-27 September 2013, Beijing, China

[12]. Montenbruck O., Gill E, Satellite Orbits Models, Methods and Applications, Springer Verlag; Edition 2000, ISBN-13 978-3540672807

[13]. R. Van Der Merwe, E. Wan, The Square-Root Unscented Kalman Filter for State and Parameter-Estimation, Acoustics, Speech, and Signal Processing, 1988. ICASSP-88., 1988 International Conference on 6:3461 - 3464 vol.6 · February 2001

[14]. Madden M. Gravity Modeling for Variable Fidelity Environments, AIAA Modeling and Simulation Technologies Conference and Exhibit; 21-24 Aug. 2006; Keystone, CO

[15]. F. Landis Markley, Attitude Error Representations for Kalman Filtering, Journal of Guidance, Control, and Dynamics, 26(2):311–317, March 2003.

[16]. Michael S. Andrle and John L. Crassidis. Geometric Integration of Quaternions, Journal of Guidance, Control, and Dynamics, Vol. 36, No. 6 (2013), pp. 1762-1767.

[17]. F. Landis Markley, Y. Cheng, J. L. Crassidis, Y. Oshman, Averaging Quaternions, Journal of Guidance, Control, And Dynamics, Vol. 30, No 4, July-August, 2007

[18]. L. Chang, B. Hu, G. Chang, Modified Unscented Quaternion Estimator Based on Quaternion Averaging, Journal of Guidance, Control, And Dynamics, Vol. 37, No 1, January-February, 2014
[19]. R. Zanetti, G. Holt, R. Gay, C. D'Souza, J. Sud, H. Mamich, M. Begley, E. King, and F. D. Clark. "Absolute Navigation Performance of the Orion Exploration Flight Test 1", Journal of Guidance, Control, and Dynamics, Vol. 40, No. 5 (2017), pp. 1106-1116. https://doi.org/10.2514/1.G002371
[20]. D. Simon, Optimal state estimation: Kalman, H infinity, and nonlinear approaches. John Wiley & Sons, 2006.
[21]. K. Yamanaka and F. Ankersen, "New state transition matrix for relative motion on an arbitrary elliptical orbit," Journal of guidance, control, and dynamics, vol. 25, no. 1, pp. 60–66, 2002.
[22]. M. Zamani, J. Trumpf, and R. Mahony, "Nonlinear attitude filtering: a comparison study," arXivpreprint arXiv:1502.03990, 2015.
[23]. A. Saccon, J. Trumpf, R. Mahony, and A. P. Aguiar, "Second-order-optimal minimum-energy filters on lie groups," IEEE Transactions on Automatic Control, Vol. 61, No. 10, 2016, pp. 2906–2919.
[24]. Y. Wu, Z. Hu, PnP problem revisited, Journal of Mathematical Imaging and Vision, vol. 24, no. 1, pp. 131-141, 2006.
[25]. C. Harris, M.A. Stephens, Combined corner and edge detector, Alvey Vision Conference, pp. 147–152, 1988.
[26]. J. Shi, C. Tomasi, Good Features to Track, IEEE Computer Society Conference on Computer Vision and Pattern Recognition, 21-23 Jun. 1994, pp. 593 – 600.
[27]. Lowe, D. G. (2004). Distinctive image features from scale-invariant keypoints. International journal of computer vision, 60(2), 91-110.
[28]. M. A. Fischler R. C. Bolles, Random sample consensus: a paradigm for model fitting with applications to image analysis and automated cartography, Communications of the ACM, vol. 24, no. 6, pp. 381–395, 1981.
[29]. V. Lepetit, F. Moreno-Noguer, P. Fua, Epnp: An accurate o (n) solution to the pnp problem, International journal of computer vision, vol. 81, no. 2, pp. 155–166, 2009.
[30]. S. Wold, K. Esbensen, P. Geladi, Principal component analysis. Chemometrics and intelligent laboratory systems, vol. 2, no. 1-3, pp. 37-52, 1987.
[31]. P. David, D. Dementhon, R. Duraiswami, H. Samet, SoftPOSIT: Simultaneous pose and correspondence determination, International Journal of Computer Vision, vol. 59, no. 3, pp. 259–284, 2004.
[32]. G. Capuano, R. Ascolese, D. Titomanlio, P. Longobardi, M. De Nino, G. Formicola, "A Multi-Ocular Smart System for Vision-based Space Navigation", 65th IAC International Astronautical Congress, Toronto (Canada), 29 September - 3 October 2014
[33]. Kaplan, E. D. & Hegarty, C. J., 2006. Understanding GPS: Principles and Applications, Artech House.
[34]. V. Capuano, E. Shehaj, P. Blunt, C. Botteron, P.-A. Farine. An adaptive GNSS-based reduced dynamic approach for real time autonomous navigation from the Earth to the Moon. Pacific PNT 2017, Honolulu, Hawaii, 2017.